J. Phys.: Condens. Matter **20** (2008) 395208 (13pp) doi:10.1088/0953-8984/20/39/395208

Electronic structure and thermodynamic properties of $Ce_3Rh_4Sn_{13}$ and $La_3Rh_4Sn_{13}$

M Gamża[1], W Schnelle[2], A Ślebarski[1], U Burkhardt[2], R Gumeniuk[2] and H Rosner[2]

[1] Institute of Physics, University of Silesia, 40-007 Katowice, Poland
[2] Max-Planck Institute for Chemical Physics of Solids, D-01187 Dresden, Germany

E-mail: andrzej.slebarski@us.edu.pl and rosner@cpfs.mpg.de

Received 19 June 2008, in final form 11 August 2008
Published 1 September 2008
Online at stacks.iop.org/JPhysCM/20/395208

Abstract

We report on the electronic structure and basic thermodynamic properties of $Ce_3Rh_4Sn_{13}$ and of the reference compound $La_3Rh_4Sn_{13}$. XPS core-level spectra revealed a stable trivalent configuration of the Ce atoms in $Ce_3Rh_4Sn_{13}$, consistent with magnetic susceptibility data. Band structure calculations within the LSDA + U approximation yield the qualitatively correct description of Ce in a trivalent state. The reliability of the theoretical results has been confirmed by a comparison of the calculated XPS valence band spectra with experimental data. The calculated densities of states as well as the rare-earth (RE) 3d XPS spectra point to a weak hybridization between the RE 4f shell and the conduction band states. The band structure calculations result in a magnetic ground state for $Ce_3Rh_4Sn_{13}$. Previous analysis pointed to the partial occupancy of the 2a site by Sn atoms. The charge density analysis reveals the dominant metallic character of the chemical bonding at the 2a atomic position. Simulation of vacancies at the 2a site using the virtual crystal approximation (VCA) indicate that the magnetic properties of $Ce_3Rh_4Sn_{13}$ strongly depend on the Sn content, which could explain the discrepancy in magnetic properties between different $Ce_3Rh_4Sn_{13}$ samples.

(Some figures in this article are in colour only in the electronic version)

1. Introduction

Detailed studies of both electronic band structure and crystal structure properties of Ce-based intermetallics are of fundamental importance for an understanding of their thermodynamic and transport characteristics. In these systems, a rich variety of unusual ground states results from the delicate balance between three types of interactions: crystal field effects, the long-range Ruderman–Kittel–Kasuya–Yosida (RKKY) coupling between the local 4f moments mediated by the conduction electrons and the on-site Kondo screening of the localized Ce 4f moments by the band states. The strengths of the last two interactions are determined by $|J_{ex}N(E_F)|$, where J_{ex} is the antiferromagnetic exchange coupling of the 4f moments with the conduction electron states and $N(E_F)$ is the density of states at the Fermi energy E_F. In the strong-coupling limit, the Kondo effect predominates and leads to a nonmagnetic ground state. At the other extreme, the RKKY interaction dominates and an ordered magnetic ground state with small discernible carrier mass renormalization results. Very interesting is the case of medium $|J_{ex}N(E_F)|$ values with the strong interplay of the Kondo and RKKY interactions. In this regime, $T_N \sim T_K$, so that both magnetic order and an enhanced electron mass can coexist and result in diverse intriguing physical phenomena, including magnetism with reduced moments, non-Fermi liquid (NFL) behaviour or unconventional superconductivity in the vicinity of the quantum phase transition from the magnetically ordered to the nonmagnetic Fermi-liquid state.

Over the past years the ternary compounds $Ce_3T_4Sn_{13}$ (T is a transition metal) have attracted considerable attention due to their heavy-fermion properties as well as peculiar crystal structure, which is closely related to the cage-type structure found in the filled skutterudites [1]. $Ce_3Ir_4Sn_{13}$ is claimed to be a heavy-fermion system ($\gamma \approx 670$ mJ mol Ce^{-1} K^{-2}) with an antiferromagnetic phase transition at $T_N = 0.6$ K [2]. In contrast, $Ce_3Co_4Sn_{13}$ does not show any sign of long-range magnetic ordering down to 0.35 K. It exhibits a short-range antiferromagnetic order at 0.8 K, which can be suppressed

by magnetic fields, giving way to single-impurity behaviour above 25 kOe with a Kondo temperature $T_K \approx 1.2$ K [3]. Interestingly, very recent studies of the new compound $Ce_3Rh_4Pb_{13}$ do not give any indication of a Kondo effect or magnetic order above 0.35 K [4]. Thus, $Ce_3Rh_4Pb_{13}$ should be located at the weakly coupled extreme of the Doniach phase diagram [5].

In view of this diversity of low-temperature physical properties in one class of isostructural and isoelectronic compounds, it is of great interest to investigate in detail another member of this family, $Ce_3Rh_4Sn_{13}$. This system is located on the periodic table in the centre among the mentioned compounds. Although it has been studied during the last few years [6–9], the results obtained by different research groups were contradictory. A single-crystal investigation revealed two successive magnetic phase transitions at $T_{N1} = 2$ K and $T_{N2} = 1.2$ K [10], while the very recent thermodynamic measurements performed on a polycrystalline sample point only to a short-range magnetic ordering at ≈1 K [11]. Furthermore, for the reference compound $La_3Rh_4Sn_{13}$ recent results revealed an intrinsic superconducting transition at 3.8 K [11], while other investigations pointed to superconductivity below 2.9 K [10] or 3.0–3.2 K [12]. Such a spread between superconducting transition temperatures as well as the contradictory reports for $Ce_3Rh_4Sn_{13}$ indicate that there is a strong sample dependence for both systems. To get an insight into its origin we prepared polycrystalline samples of both $Ce_3Rh_4Sn_{13}$ and $La_3Rh_4Sn_{13}$. We characterized the samples carefully by powder x-ray diffraction (XRD) analysis and both energy-dispersive x-ray (EDX) and wavelength-dispersive x-ray (WDX) microanalysis.

In this contribution we present a combined study of the electronic structure and basic thermodynamic properties of the compounds $Ce_3Rh_4Sn_{13}$ and $La_3Rh_4Sn_{13}$. We decided to remeasure the magnetic susceptibility, specific heat and electrical resistivity in order to clarify the magnetic/superconducting properties. To gain deeper insight into the character of the Ce 4f states in $Ce_3Rh_4Sn_{13}$ we carried out x-ray photoemission spectroscopy (XPS) experiments. Based on the rare-earth (RE) core-level spectra we analyse the hybridization strength between the RE 4f shell and the conduction band states for both $Ce_3Rh_4Sn_{13}$ and $La_3Rh_4Sn_{13}$. The XPS valence band spectra we interpret with the help of *ab initio* band structure calculations. We performed a computational crystal structure optimization to compare the experimental data with theoretical estimations for the stoichiometric compounds $Ce_3Rh_4Sn_{13}$ and $La_3Rh_4Sn_{13}$. Previous findings [6, 7] pointed to the partial occupancy of the 2a site by Sn atoms in both investigated compounds. To explore its reason we analyse chemical bonding based on the valence and difference charge density maps. Finally, we simulate vacancies in the 2a atomic position using band structure calculations within the virtual crystal approximation (VCA) and investigate the influence of the vacancies on the magnetic properties of $Ce_3Rh_4Sn_{13}$.

2. Methods

2.1. Experimental details

Polycrystalline samples of $Ce_3Rh_4Sn_{13}$ and $La_3Rh_4Sn_{13}$ were prepared by arc melting of the elements (Ce 99.99 wt%, La 99.99 wt%, Rh 99.95 wt%, Sn 99.995 wt%) in the atomic ratio 3:4:13 on a water-cooled cooper hearth in a high purity Ar atmosphere with an Al getter (heated above the melting point). Both samples were remelted several times to promote homogeneity and annealed at 870 °C for 14 d in an evacuated quartz tube. Almost no mass loss (⩽0.02%) occurred during the melting and annealing processes. Powder XRD patterns were collected at room temperature on a Siemens D-5000 diffractometer (Cu Kα radiation, 2θ range 15°–100°, step 0.02°, scanning time 7 s for each angle). Phase analysis was carried out by comparison of experimentally obtained powder patterns with theoretically calculated patterns using the POWDER-CELL programme [13]. Lattice parameters were refined by least-squares fittings of the XRD patterns using the WinCSD program package [14].

The microstructures of the $Ce_3Rh_4Sn_{13}$ sample were investigated by WDX analyses on a CAMECA SX100 electron microprobe with a tungsten cathode. The local composition was determined by intensities of the x-ray lines CeL, SnL and RhL which were excited by an electron beam of 25 keV/10 nA and 25 keV/40 nA, respectively. The x-ray lines were focused by large monochromator crystals PET (Pentaerythritol, $d = 0.437$ nm) on a gas flow proportional counter. The proportions of the three elements were determined with respect to the appropriate reference material Rh, Sn and $CeAl_2$. After matrix correction and final averaging on ten points the summation of all three contributions (Ce: 18.7(4) wt%, Rh: 17.41(7) wt%, Sn: 66.1(6) wt%) results in the total value of 102(1)%. The calculation from the normalized value gives the following contents: Ce: 15.5(3) at.%, Rh: 19.7(1) at.% and Sn: 64.8(4) at.%.

Standardless EDX analyses were performed on the same sample and on the homoeotypic $La_3Rh_4Sn_{13}$ phase. The x-ray spectra have been recorded by an Si(Li) detector of the EDAX (Ametek) system attached to the microprobe. The acceleration voltage of 25 keV was used and led to the following compositions:

Ce: 15.5 at.% Rh: 20.3 at.% Sn: 64.2 at.%
La: 16.0 at.% Rh: 20.3 at.% Sn: 63.7 at.%.

XPS spectra were obtained with monochromatized Al Kα radiation at room temperature using a PHI 5700 ESCA spectrometer. Polycrystalline samples were broken under a high vacuum of 6×10^{-10} Torr immediately before taking spectra. Calibration of the spectra was performed according to [15]. Binding energies were referenced to the Fermi level ($E_F = 0$).

The magnetization was measured in a SQUID magnetometer (MPMS XL-7, Quantum Design) in magnetic fields 20 Oe $\leqslant H \leqslant$ 70 kOe between 1.8 and 400 K. Heat capacity was determined by a relaxation-type method (PPMS, Quantum Design). Electrical resistivity measurements were performed on polycrystalline pieces with a standard dc four-probe set-up.

Table 1. Comparison of the structural data from experiment, LDA and LSDA + U ($U = 6$ eV) calculations for $Ce_3Rh_4Sn_{13}$ and $La_3Rh_4Sn_{13}$. The theoretically obtained lattice parameters and internal positions were rounded to 2 and 3 significant digits, respectively.

Lattice parameter a (Å)		
$La_3Rh_4Sn_{13}$	$Ce_3Rh_4Sn_{13}$	Data from
9.7521(6)	9.7117(2)	Our data
9.745(1)	9.708(1)	[7]
9.745	9.710	[8]
—	9.7051(3)	[9]
9.70	9.61	LDA
—	9.60	LSDA + U

Atomic positions				
Atom	Wyckoff site	x	y	z
RE	6d	0.25	0.5	0
Rh	8e	0.25	0.25	0.25
Sn1	2a	0	0	0
Sn2	24k	0	y_{Sn2}	z_{Sn2}

	Compound					
	$La_3Rh_4Sn_{13}$		$Ce_3Rh_4Sn_{13}$			
	[7]	LDA	[9]	[7]	LDA	LSDA + U
y_{Sn2}	0.305 55(10)	0.306	0.3080(2)	0.3070(2)	0.309	0.304
z_{Sn2}	0.153 76(6)	0.153	0.1541(2)	0.1537(1)	0.152	0.152

The ac magnetic susceptibility data were collected in the temperature range of 1.8–300 K using a Lake-Shore ac susceptometer. The amplitude of the excitation field was 10 Oe at a fixed frequency of 10 kHz.

2.2. Computational

The electronic structure of both $Ce_3Rh_4Sn_{13}$ and $La_3Rh_4Sn_{13}$ is studied using the full potential local orbital (FPLO) minimum basis code (version 5.00-19) [16] within the local spin density approximation (LSDA). In the scalar-relativistic calculations the exchange–correlation (XC) potential of Perdew and Wang was employed [17]. As a basis set, Ce(4f5s5p/5d6s6p), La(5s5p/5d6s6p: 4f), Rh(4s4p/4d5s5p) and Sn(4s4p4d/5s5p: 5d) states were employed as semi-core/valence: polarization states. The lower-lying states were treated fully relativistically as core states. The inclusion of semi-core states was extorted by their non-negligible overlap with orbitals on neighbouring atoms which results in a non-negligible bandwidth. The La 4f and Sn 5d states were taken into account as polarization states to improve the completeness of the basis set. The spatial extension of the basis orbitals, controlled by the confining potential $(r/r_0)^n$ with $n = 5$, was optimized to minimize the total energy [18]. The strong Coulomb correlation within the Ce 4f shell was treated in a mean field approximation using the LSDA + U method [19] (applying the around mean field double counting scheme). The Coulomb repulsion U and on-site exchange J for the Ce 4f states were assumed to be 3–8 eV and 0–1 eV, respectively. The Brillouin zone was sampled by a k-mesh containing 84 irreducible points.

To analyse the topology of the valence charge density we performed also band structure calculations by the full potential linearized augmented plane-wave (FP-LAPW) method [20] using the WIEN2k_05 computer code [21]. The resulting electronic densities of states and band structures were basically identical for the two band structure codes.

Based on the band structure results we calculated the theoretical XPS valence band spectra. The partial l-resolved densities of states were multiplied by the corresponding cross sections [22] and convoluted by the Lorentzians with a full width at half-maximum of 0.4 eV to account for the instrumental resolution, thermal broadening and the effect of the lifetime of the hole states. The results were convoluted by the Fermi–Dirac function for 300 K.

3. Results and discussion

3.1. Sample characterization

In the 1980s and early 1990s, considerable attention was devoted to the distortion of this structure in the $RE_3Rh_4Sn_{13}$ series, which was observed in samples after crystal growth [7, 23, 8]. The results, however, were controversial.

Comparison of theoretically calculated intensities in XRD patterns with those obtained experimentally as well as refined lattice parameters (table 1) confirm $Ce_3Rh_4Sn_{13}$ and $La_3Rh_4Sn_{13}$ to crystallize within the $Yb_3Rh_4Sn_{13}$ structure type (space group: $Pm\bar{3}n$), which is consistent with the refinement performed by Niepmann *et al* [6]. Since no unidentified reflections in these patterns were observed, we conclude that, if any distortion takes place then it is only at annealing temperatures lower than 870 °C.

The $Ce_3Rh_4Sn_{13}$ sample was found to be nearly single-phased. The phase analysis performed on the XRD patterns revealed only a small amount of Sn impurity. For the sample of the reference compound $La_3Rh_4Sn_{13}$ the Sn content was approximately four times larger. The EDX analysis of both

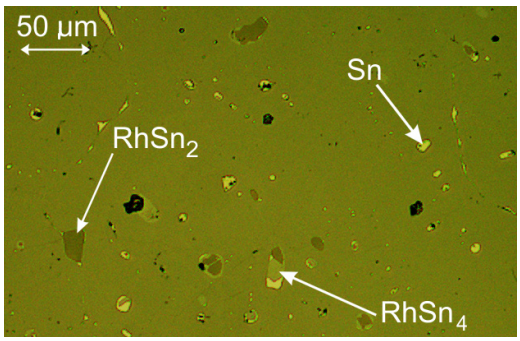

Figure 1. (Colour online) Metallographic microstructure with small amounts of minority phases in the $Ce_3Rh_4Sn_{13}$ majority phase (light optical image, bright-field contrast, $Ce_3Rh_4Sn_{13}$ sample, 870 °C/14 d).

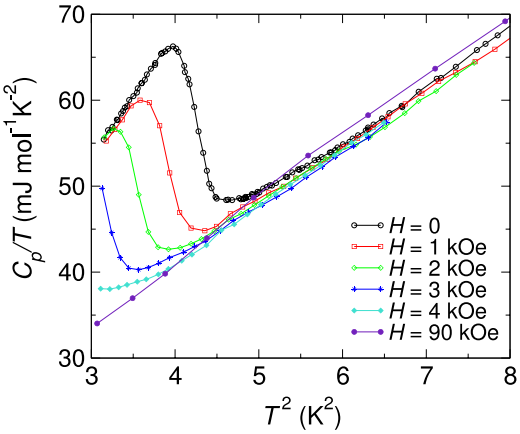

Figure 2. (Colour online) Low-temperature specific heat of $La_3Rh_4Sn_{13}$ measured with and without an external magnetic field, plotted in a conventional C_p/T versus T^2 presentation.

$La_3Rh_4Sn_{13}$ and $Ce_3Rh_4Sn_{13}$ samples shows that there are also few grains of the phase $RhSn_2$. Some Sn particles are accompanied also by a small amount of $RhSn_4$ phase in the $Ce_3Rh_4Sn_{13}$ sample (figure 1).

In order to verify the composition of the main phase in the $Ce_3Rh_4Sn_{13}$ sample we performed both EDX and WDX studies at several points of the polished surface. The average composition was found to be $Ce_{15.5(3)}Rh_{19.7(1)}Sn_{64.8(4)}$, which corresponds to $Ce_{3.10(7)}Rh_{3.94(2)}Sn_{12.96(8)}$ and is in agreement with stoichiometric $Ce_3Rh_4Sn_{13}$. For the $La_3Rh_4Sn_{13}$ sample the composition of the majority phase determined by the EDX investigations after averaging on three points corresponds to $La_{3.2(1)}Rh_{4.1(1)}Sn_{12.7(1)}$.

The distinct Sn fraction in the $La_3Rh_4Sn_{13}$ sample suggests that there is a small deviation of the nominal composition of the majority phase from the ideal 3:4:13 atomic ratio, since almost no mass losses (<0.05%) were observed during melting and annealing of the sample which had the initial composition $La_3Rh_4Sn_{13}$. Previously, Niepmann *et al* [6] pointed to the partial occupancy of Sn at the 2a site of 92% for the system $Ce_3Rh_4Sn_{13}$ based on the thermal parameters obtained from single-crystal structure refinement. A similar conclusion could be derived from the data reported in [7] for both $La_3Rh_4Sn_{13}$ and $Ce_3Rh_4Sn_{13}$. These findings corroborate our results and indicate that the investigated compounds have some homogeneity range related to the partial occupancy of the 2a site by Sn atoms. On the other hand, the lattice parameters for both $Ce_3Rh_4Sn_{13}$ and $La_3Rh_4Sn_{13}$, determined from the powder diffraction patterns, do not differ significantly from those previously reported (table 1) and are in good agreement with those obtained from the computational crystal structure optimization for the stoichiometric compounds (see the discussion in section 3.4). More extended studies are required to establish the possible homogeneity range for these systems.

3.2. Thermodynamics

3.2.1. Specific heat. The temperature dependence of the specific heat for $La_3Rh_4Sn_{13}$ above 4 K is typical for a nonmagnetic metal (not shown). The experimental data between 4 and 10 K follow the dependence

$$C_p = \gamma T + \beta T^3 \qquad (1)$$

with the Sommerfeld coefficient $\gamma \approx 13.5$ mJ mol^{-1} K^{-2} and $\beta \approx 7.5$ mJ mol^{-1} K^{-4}. The estimated γ and β values are slightly higher than those previously reported [10]. Using $\beta = (12/5)Rn\pi^4\theta_D^{-3}$, where n is the number of atoms in a formula unit and R is the gas constant, we find the initial Debye temperature $\theta_D = 173$ K.

At lower temperatures, there is a distinct anomaly in the temperature dependence of the specific heat for $La_3Rh_4Sn_{13}$. Figure 2 shows the low-temperature data measured in several magnetic fields plotted in the conventional C_p/T versus T^2 presentation. A clear step, which shifts towards lower temperatures with increasing magnetic field, points to the intrinsic superconducting phase transition. The critical temperature $T_c = 2.07$ K is significantly lower than in previous reports [11, 10, 12]. Magnetic fields of the order of 10 kOe completely suppress the superconductivity of $La_3Rh_4Sn_{13}$. The large value of the ratio $\Delta C_p/(\gamma T_c) \approx 2$, where ΔC_p is the estimated magnitude of the jump in C_p at the transition temperature, might suggest that the investigated compound is a strongly coupled superconductor. To verify this finding and estimate the phonon–electron coupling parameter λ we use the McMillan formula

$$T_c = \frac{\theta_D}{1.45}\exp\left\{\frac{-1.04(1+\lambda)}{\lambda-\mu^*(1+0.62\lambda)}\right\}, \qquad (2)$$

where μ^* is the Coulomb pseudopotential whose value was chosen to be 0.1, as is typical for s and p band superconductors. This yields $\lambda \approx 0.6$, which negates the strong-coupling superconductivity in $La_3Rh_4Sn_{13}$. C_p/T versus T^2 for temperatures above T_c exhibits a slight field dependence and some deviation from linearity expected for a nonmagnetic metal. We ascribe this behaviour to an additional superconducting contribution of the Sn impurities in the polycrystalline sample ($T_c \approx 3.7$ K), which were detected by the EDX and XRD investigations.

For $Ce_3Rh_4Sn_{13}$, the specific heat experiments do not give any evidence of a magnetic phase transition down to the lowest measuring temperature of 1.8 K, in contrast to the results reported by Ōduchi *et al* [10]. At temperatures below

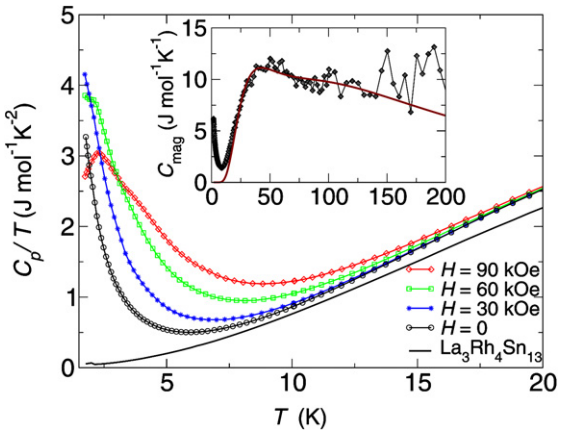

Figure 3. (Colour online) Specific heat divided by temperature C_p/T versus T for $Ce_3Rh_4Sn_{13}$ and for the nonmagnetic reference compound $La_3Rh_4Sn_{13}$. The inset shows the magnetic part of the specific heat C_{mag} of $Ce_3Rh_4Sn_{13}$ accompanied by the fit to the multi-Schottky anomaly with $\Delta_1/k_B = 90$ K and $\Delta_2/k_B = 350$ K.

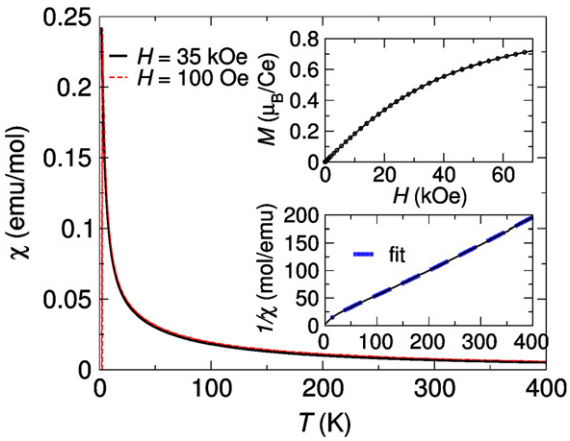

Figure 4. (Colour online) Magnetic susceptibility χ of $Ce_3Rh_4Sn_{13}$ in external fields of 100 Oe and 35 kOe. The upper inset displays magnetization versus external field measured at $T = 2$ K. The lower inset shows the inverse of magnetic susceptibility collected in a field of 35 kOe. The fit using the Van Vleck formula covers the χ^{-1} curve in a temperature range of 12–400 K.

5 K, there is a pronounced upturn in C_p/T values measured without external magnetic field (figure 3), perhaps indicative of an incipient order. The application of magnetic fields shows that this is the high-temperature side of a wide peak, that broadens and shifts to higher temperatures with increasing magnetic field. Recently, a very similar behaviour of the low-temperature specific heat for polycrystalline $Ce_3Rh_4Sn_{13}$ was found by Köhler *et al* [11]. Their detailed analysis based on specific heat and ac susceptibility data pointed to short-range antiferromagnetic order at $T \approx 1$ K. At higher magnetic fields the peak in specific heat can be attributed to a Schottky anomaly caused by excitations between the Zeeman levels of the ground state doublet.

For the tetragonal point symmetry of Ce the sixfold degenerated Hund's rule multiplet of Ce^{3+} ions ($J = 5/2$) splits into three Kramer doublets. To isolate the Ce 4f-derived part of the specific heat $C_{mag}(T)$ of $Ce_3Rh_4Sn_{13}$ we assumed that the lattice heat capacity of $Ce_3Rh_4Sn_{13}$ is the same as that of the isostructural reference compound $La_3Rh_4Sn_{13}$. Thus we subtracted from the total specific heat of $Ce_3Rh_4Sn_{13}$ the corresponding data of $La_3Rh_4Sn_{13}$. The result is shown in the inset of figure 3.

$C_{mag}(T)$ shows a prominent broad feature with a maximum at about 40 K, which can be well described by a multi-Schottky anomaly resulting from thermally activated transitions from a ground state doublet to the higher-lying states. The best fit has been achieved assuming that the two excited doublets are separated from the ground state by the energy gaps $\Delta_1/k_B \approx 95$ K and $\Delta_2/k_B \approx 350$ K. Such a splitting of the $J = 5/2$ multiplet agrees well with the recent findings of an inelastic neutron scattering experiment [24]; only the energy position of the highest doublet is slightly lower than those from the neutron studies. This can be attributed to the large uncertainties of C_{mag} in the high-temperature region.

The ground state magnetic specific heat ($C_{mag} - C_{Schottky}$) shows an extended tail up to the temperature of 20 K, which arises from magnetic precursor effects [25] (see the discussion in section 3.7).

The specific heat of $Ce_3Rh_4Sn_{13}$ does not exhibit any feature at 3.7 K, which could be attributed to the superconductivity of the Sn impurities. This is in line with the XRD analysis (see section 3.1) which detected only traces of elemental Sn in the $Ce_3Rh_4Sn_{13}$ sample.

3.2.2. Magnetic susceptibility. Figure 4 shows the results of the dc magnetic susceptibility measurements for the compound $Ce_3Rh_4Sn_{13}$. We collected the magnetic susceptibility data in a temperature range of 1.8–400 K at magnetic fields from 100 Oe up to 35 kOe. The results recorded for increasing temperatures after zero-field-cooling are identical with the field-cooling data within experimental errors. There is no evidence for a magnetic phase transition down to 1.8 K in the susceptibility curves, in agreement with heat capacity results. The shape of the $\chi(T)$ curves almost does not depend on the applied magnetic field apart from low temperatures (below ≈12 K). At temperatures above 150 K the susceptibility might be described by a modified Curie–Weiss law:

$$\chi = \chi_0 + \frac{C}{T - \theta}, \tag{3}$$

where χ_0 is the temperature-independent part of the magnetic susceptibility, θ is the paramagnetic Curie temperature and C is the Curie constant. The least-squares fit to the data in the temperature range of 150–400 K yields $\chi_0 = -0.000\,54$ emu mol^{-1}, $\theta = -29$ K and $C = 2.413$ emu K mol^{-1}: thus, the effective Ce magnetic moment is $\mu_{eff} = 2.53\ \mu_B$/Ce. This result is close to the theoretical value of 2.54 μ_B/Ce expected for a free Ce^{3+} ion, indicating that the magnetic moments of Ce ions in $Ce_3Rh_4Sn_{13}$ are well localized at high temperatures and the other atoms (Rh and Sn) do not carry magnetic moments. The significant negative θ value results primarily from the crystal electric field splitting.

At lower temperatures the inverse of χ deviates strongly from the Curie–Weiss-type straight line in a manner which

suggests a thermal depopulation of the excited crystal field levels associated with the $4f^1$ Ce ion. For temperatures above 12 K, the experimental $\chi^{-1}(T)$ curves measured at magnetic fields above 1 kOe can be well described in terms of the crystal electric field model. For the tetragonal Ce point symmetry, where the $J = 5/2$ multiplet of Ce^{3+} ions splits into three doublets, the Van Vleck formula supplemented by the temperature-independent contribution χ_0 takes the form

$$\chi(T) = \frac{9}{8}\left[a/T + b + (c/T + d)\exp\left(-\frac{\Delta_1}{T}\right) + (e/T - b - d)\exp\left(-\frac{\Delta_2}{T}\right)\right]\left[2 + 2\exp\left(-\frac{\Delta_1}{T}\right) + 2\exp\left(-\frac{\Delta_2}{T}\right)\right]^{-1} + \chi_0, \quad (4)$$

where a, c and e are the low-frequency matrix elements, while b and d are the high-frequency contributions. We assumed that the two excited doublets are separated from the ground state by the energy gaps, as indicated by the heat capacity data. Fitting equation (4) to the experimental data in a temperature range of 10–400 K yields the following parameters: $a = 1.19\ \mu_B^2$, $b = 0.04\ \mu_B^2\ K^{-1}$, $c = 1.28\ \mu_B^2$, $d = -0.02\ \mu_B^2\ K^{-1}$, $e = 0.91\ \mu_B^2$ and $\chi_0 = -0.00023$ emu mol^{-1}.

Below the temperature of 12 K, $\chi^{-1}(T)$ exhibits a pronounced downward curvature. For a system which does not show magnetic order, this may hint at a substantial Kondo screening effect.

In a weak magnetic field (∼100 Oe) one can clearly see a strong diamagnetic signal below ≈3 K due to the superconductivity of the Sn impurities in the sample. This contribution is suppressed by a magnetic field of 400 Oe. An estimation of the amount of Sn impurities in the sample based on the Meissner and shielding effects yields less than 2% of the sample volume. The fit of the modified Curie–Weiss law to the low-temperature low-field data (below 10 K) results in a θ value of −0.64 K, which corroborates the small amplitude of antiferromagnetic exchange interaction corresponding to the ground state doublet.

Recently we have found that some compounds of the series of Ce–Rh–Sn intermetallics show the sign of spin fluctuations due to the Rh 4d electrons [26, 27]. In order to investigate possible spin fluctuations in $Ce_3Rh_4Sn_{13}$ we have carried out ac magnetic susceptibility measurements down to a temperature of 2 K. The ac susceptibility curve (not shown) does not give any evidence for magnetic ordering and does not exhibit any feature that could be attributed to charge or spin fluctuation effects. This finding rules out the possibility of spin fluctuations owing to Rh 4d electrons and supports the stable valence of Ce ions in $Ce_3Rh_4Sn_{13}$.

The upper inset of figure 4 displays the isothermal magnetization at $T = 2$ K for $Ce_3Rh_4Sn_{13}$ plotted as a function of external field. The data collected with increasing and decreasing field strengths do not show distinct hysteresis. The overall shape of the $M(H)$ curve is consistent with what one expects for the influence of a magnetic field on the paramagnetic Ce ions at 2 K. For the highest available field of 70 kOe the magnetic moment of Ce reaches only 0.72 μ_B/Ce and does not saturate. An extrapolation of $M(1/H)$ to $1/H = 0$ yields 0.96 μ_B/Ce, much less than the theoretical saturation moment $gJ = 2.14\ \mu_B$ for the free Ce^{3+} ions, as should be expected for a system with large crystal field splitting of the ground state multiplet.

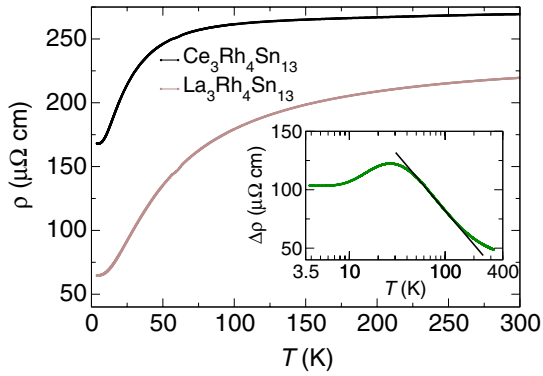

Figure 5. (Colour online) Resistivity of $Ce_3Rh_4Sn_{13}$ and $La_3Rh_4Sn_{13}$. The inset shows the magnetic part of the resistivity $\Delta\rho$ of $Ce_3Rh_4Sn_{13}$ versus log T.

The magnetic susceptibility of $La_3Rh_4Sn_{13}$ (not shown) is negative and shows only a slight temperature dependence in strong magnetic fields (>10 kOe). After correction for ferromagnetic and paramagnetic impurities, an extrapolation of $\chi(T)$ to $T = 0$ K results in $\chi_0 \approx -840 \times 10^{-6}$ emu mol^{-1}. For comparison, the sum of the diamagnetic increments for the closed-shell ions was calculated. Diamagnetic core increments used are $\chi_{dia}(Sn^{4+}) = -16 \times 10^{-6}$ emu mol^{-1} for tin, $\chi_{dia}(La^{3+}) = -20 \times 10^{-6}$ emu mol^{-1} for lanthanum and $\chi_{dia}(Rh^{4+}) = -18 \times 10^{-6}$ emu mol^{-1} for rhodium [28]. Such an estimation gives the value of -340×10^{-6} emu mol^{-1}, which is much smaller than the obtained χ_0 value. Thus, taking into account that there must also be an additional positive contribution included in the measured susceptibility due to the magnetism of conduction electrons, $La_3Rh_4Sn_{13}$ is supposed to be strongly diamagnetic.

In low fields there is a pronounced downwards curvature in $\chi(T)$ curves which starts around 3 K and is probably related to the Sn impurities in the sample. There is also a strong diamagnetic contribution below 2.1 K, which can be assigned to the superconducting phase transition detected by the specific heat analysis.

3.2.3. Electrical resistivity. Figure 5 shows the temperature dependence of the electrical resistivity of $Ce_3Rh_4Sn_{13}$ and $La_3Rh_4Sn_{13}$.

$La_3Rh_4Sn_{13}$ exhibits metallic behaviour in the whole investigated temperature range of 3.8–300 K. Below 8 K the resistivity follows a T^5 dependence, which is characteristic of phonon scattering. At higher temperatures there is a significant departure from the behaviour which one would expect from the Bloch–Grüneisen description. The clear shoulder around 70 K could be attributed to the interband s–d scattering of the conduction electrons [29], which is often observed for intermetallic compounds with transition metal atoms. The rather large value of the residual resistivity at 4 K and the small value of the ratio $\rho(300\ K)/\rho(4\ K) \approx 3.5$ are in line with

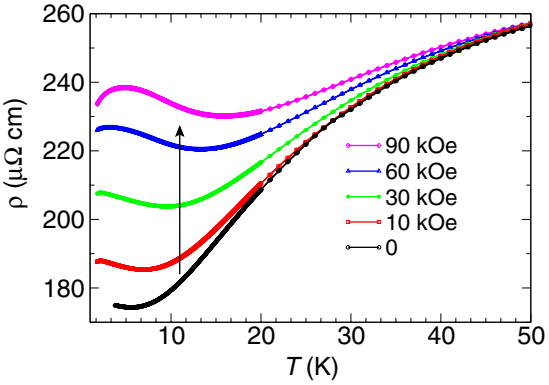

Figure 6. (Colour online) Magnetoresistivity of $Ce_3Rh_4Sn_{13}$ in different external fields.

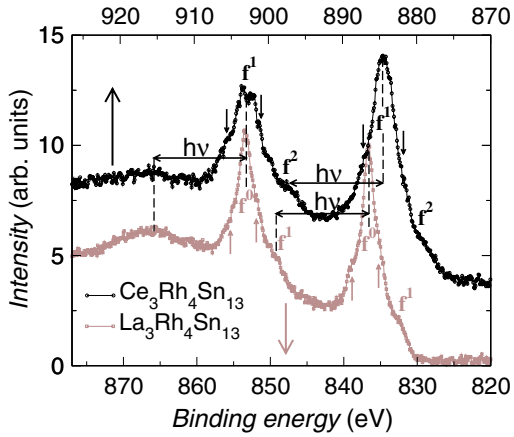

Figure 7. (Colour online) The RE 3d XPS spectra for $Ce_3Rh_4Sn_{13}$ and $La_3Rh_4Sn_{13}$. The f^n and f^{n+1} contributions are signed, while plasmon resonance structures are indicated by horizontal arrows. Plasmon energy $h\nu \approx 13$ eV. Vertical arrows point to the shoulders originating from Ce_2O_3 and La_2O_3.

the substantial amount of disorder and the existence of many structural defects in the investigated sample.

For $Ce_3Rh_4Sn_{13}$, the zero-field resistivity shows a rather weak temperature dependence with a slight minimum at 5 K and a pronounced shoulder around 70 K. At higher temperatures $\rho(T)$ almost saturates at the large value of 265 $\mu\Omega$ cm. The slight increase in resistivity below 5 K can be attributed to the magnetic scattering related to the incipient (presumably short-range) magnetic ordering, as suggested by the specific heat results (see in section 3.2.1). In order to estimate the Ce 4f-derived part of the resistivity, we assumed that the lattice contribution is given by the $\rho(T)$ of the nonmagnetic isostructural compound $La_3Rh_4Sn_{13}$ and we subtracted the corresponding data from those of the $Ce_3Rh_4Sn_{13}$. The result, denoted as $\Delta\rho(T)$, is presented in the inset of figure 5. A broad maximum in the magnetic resistivity at a temperature of 30 K can be associated with the crystal field effect, since the heat capacity measurements revealed a Schottky anomaly at similar temperatures. Above 50 K, one can see a logarithmic temperature dependence up to 130 K, which might be indicative for incoherent Kondo scattering. The least-squares fit of the $\Delta\rho(T)$ data in this temperature range to the Kondo formula, $\Delta\rho(T) = \rho_0' - c_k \ln T$, where ρ_0' includes first of all a large spin-disorder component, yields for the Kondo coefficient c_k the value of 48 $\mu\Omega$ cm K^{-1}, thus hinting at an enhanced density of states at the Fermi level. This kind of behaviour of magnetic resistivity is typical for Ce-based Kondo systems with strong crystal field [30]. On the other hand, one should note that the temperature dependence of the resistivity may be affected by the impurity phases detected in the sample, so that a considerable part of ρ might not be intrinsic.

To get further insight into the electron scattering in $Ce_3Rh_4Sn_{13}$ we have studied the influence of a magnetic field on the electrical resistivity by measuring magnetoresistance. Figure 6 shows $\rho(T, H)$ with field perpendicular to the current. The maximum which appears at a few K can be attributed to the scattering on the Zeeman split of the crystal field ground state doublet, since the temperature of the maximum in magnetoresistivity coincides with the field dependence of the low-temperature Schottky-like anomaly found in $C_p(T)$. We observe also a large positive contribution to the magnetoresistivity below ≈50 K, which increases with applied magnetic field. Its origin will be discussed in section 3.7.

3.3. RE core-level XPS spectra

Analysis of the RE core-level XPS spectra is an efficient tool for getting insight into the character of RE 4f states in intermetallics owing to the strong Coulomb interaction between the photoemission core hole and the electrons in the vicinity of the Fermi level. This coupling results in complex structures of the RE core-level XPS spectra. The detailed analysis we restrict to the most intensive peaks related to photoemission from RE 3d and 4d states because of the lifetime broadening for the other levels which masks fine structures originating from screening effects.

Figure 7 shows the RE 3d XPS spectra of $Ce_3Rh_4Sn_{13}$ and $La_3Rh_4Sn_{13}$ taken at an excitation photon energy of 1486.6 eV (Al Kα). Due to the spin–orbit (SO) interaction there are two sets of RE 3d photoemission lines in each spectrum, which are attributed to the $3d_{3/2}$ and $3d_{5/2}$ components of the final states, with intensity ratio $I(3d_{5/2})/I(3d_{3/2}) = 3/2$. The estimated values of the SO splitting ($\delta_{Ce} \approx 18.6$ eV, $\delta_{La} \approx 17.3$ eV) are in agreement with those obtained from the *ab initio* band structure calculations ($\delta_{Ce} \approx 18.83$ eV and $\delta_{La} \approx 17.22$ eV).

Each SO set of the RE 3d photoemission lines consists of two contributions labelled as f^n and f^{n+1}, where $n = 0$ or $n = 1$ for La and Ce, respectively. These peaks arise from different screening mechanisms. The main components of the 3d lines f^n appear when the core hole is screened by conduction electrons. The f^{n+1} satellites, located on the low-energy side of the main peaks, result from a $4f^n \rightarrow 4f^{n+1}$ transition during the photoemission process. Thus, the core hole becomes screened by an extra 4f electron in an exciton-like level centred on the core-ionized atom. The probability of transferring an electron to this screening level depends critically on its coupling to the other occupied states. Consequently, the f^{n+1} contributions

in the measured RE 3d XPS spectra reflect the degree of hybridization between the 4f and conduction band states in the initial state.

One should note that the main photoemission lines in RE 3d XPS spectra are wider for $Ce_3Rh_4Sn_{13}$ than for the reference compound $La_3Rh_4Sn_{13}$. The observed broadening results from multiplet effects, which are absent in the La f^0 peaks, as well as a special broadening mechanism related to the so-called virtual-bound-state effects [31]. The last mechanism arises because the state from which an electron hops into a localized 4f screening orbital from the other valence states is energetically degenerated with a poorly screened state.

In addition, the RE 3d XPS spectra of both $Ce_3Rh_4Sn_{13}$ and $La_3Rh_4Sn_{13}$ show similar broad features at a distance of ≈13 eV from the main photoemission lines. We interpret these peaks as plasmon resonance structures arising from collective oscillations of conduction electrons, as indicated in figure 7. Very similar energy loss lines have been observed recently for the compounds $RERhSn_2$ [26] and $Ce_5Rh_4Sn_{10}$ [32]. In the spectrum of $La_3Rh_4Sn_{13}$ the plasmon satellite at a binding energy of 866 eV overlaps with the La MNN Auger line.

In the RE 3d XPS spectra of $RE_3Rh_4Sn_{13}$ there are also slight shoulders, which we indicated in figure 7 by short vertical arrows. Since their intensity was increasing for the low-angle measurements and as the time after sample breaking went by, they are assigned to the surface oxidation during measurements. Indeed, these additional contributions correspond to the RE 3d photoemission lines of Ce_2O_3 and La_2O_3, respectively. One should note that, in the case of the compound $Ce_3Rh_4Sn_{13}$, the Ce 3d photoemission lines also overlap with a small peak originating from the Sn 3s states which are located at a binding energy of 885 eV.

We did not find any additional, sharp peaks in the Ce 3d XPS spectrum at a distance of ∼11 eV from the main photoemission lines which could be assigned to the Ce $3d^9f^0$ final state, giving evidence of an intermediate valence behaviour of Ce in $Ce_3Rh_4Sn_{13}$. This result is consistent with the magnetic susceptibility data discussed in section 3.2.2.

The stable valence of Ce ions has also been confirmed by the Ce 4d XPS spectrum (figure 8), where we observe only a broad structure at binding energies ranging from 104 to 118 eV, similar to that found in the La 4d spectrum. These complexes consist of two sets of photoemission lines originating from $4d^94f^n$ and $4d^94f^{n+1}$ final states, whose separation corresponds to the core-hole 4d spin–orbit interaction: $\delta_{Ce} \approx 3.2$ eV and $\delta_{La} \approx 3.0$ eV. These values of the SO splitting for both $Ce_3Rh_4Sn_{13}$ and $La_3Rh_4Sn_{13}$ are consistent with the theoretical estimates: $\delta_{Ce} \approx 3.32$ eV and $\delta_{La} \approx 2.98$ eV. In the case of photoemission from Ce the detailed analysis of this region is not possible due to the strong exchange interaction between 4d holes and the unfilled 4f levels, which gives rise to complicated multiplet structures [33].

The Ce 4d XPS spectra for intermediate valence systems show distinct contributions due to the $4d^94f^0$ final states. These peaks are usually observed at a distance of 11 eV from the main photoemission lines and their splitting is almost equal to the 4d spin–orbit splitting in La (≈2.9 eV) [34, 35, 33]. The Ce 4d XPS spectrum of $Ce_3Rh_4Sn_{13}$ does not give any

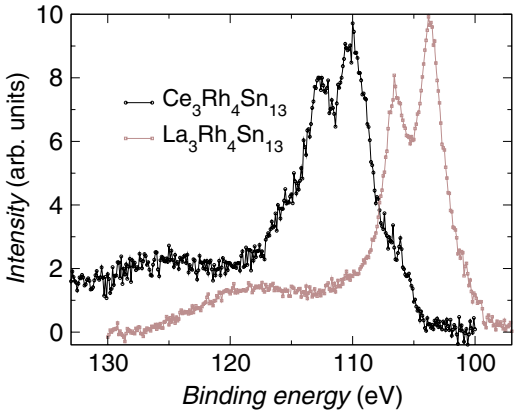

Figure 8. (Colour online) The RE 4d XPS spectra for $Ce_3Rh_4Sn_{13}$ and $La_3Rh_4Sn_{13}$.

evidence for additional peaks at a binding energy of 118–124 eV, which could be attributed to $4d^94f^0$ final states. In RE 4d XPS spectra for both $La_3Rh_4Sn_{13}$ and $Ce_3Rh_4Sn_{13}$ there are only similar broad features at a distance of 13 eV from the main photoemission structures, which can be assigned to plasmon-loss satellites.

In order to estimate the hybridization strength between the 4f and conduction band states we performed the quantitative analysis of the RE 3d XPS spectra based on the Gunnarsson and Schönhammer model calculations [34, 36]. Details of the method have been described elsewhere [32]. The same procedure has been applied for both $La_3Rh_4Sn_{13}$ and $Ce_3Rh_4Sn_{13}$. For the parameter Δ, which describes the hybridization part of the Anderson impurity Hamiltonian and reflects the hybridization strength between the RE 4f shell and conduction electron states, we obtained about 35 meV and 50 meV for $Ce_3Rh_4Sn_{13}$ and $La_3Rh_4Sn_{13}$, respectively. This result is consistent with the general finding that hybridization tends to be smaller in Ce compounds than in their La counterparts due to the larger contraction of the 4f orbitals in Ce.

The estimated hybridization energy Δ for $Ce_3Rh_4Sn_{13}$ is rather small, much smaller than the typical Δ values for Ce-based intermediate valence compounds (100–160 meV) [37, 34]. This result is in line with the stable valence of Ce ions in the investigated system and points to the well-localized character of the Ce 4f states. It should be stressed, however, that such a hybridization is found to be sufficient for the formation of a Kondo lattice state, e.g. for the heavy-fermion superconductor $CeCu_2Si_2$ [38].

3.4. Valence band

Figure 9 shows the total and partial atom-resolved densities of states (DOS) for $Ce_3Rh_4Sn_{13}$ and $La_3Rh_4Sn_{13}$ calculated within the LDA approximation. We also performed spin-polarized band structure calculations for both compounds (not shown). The results revealed a magnetic ground state for $Ce_3Rh_4Sn_{13}$ with significant magnetic moments of 0.2 μ_B only at Ce atoms, while $La_3Rh_4Sn_{13}$ is expected to be nonmagnetic.

The characteristic feature of the DOSs for $Ce_3Rh_4Sn_{13}$ are narrow bands pinned at the Fermi level E_F. These bands

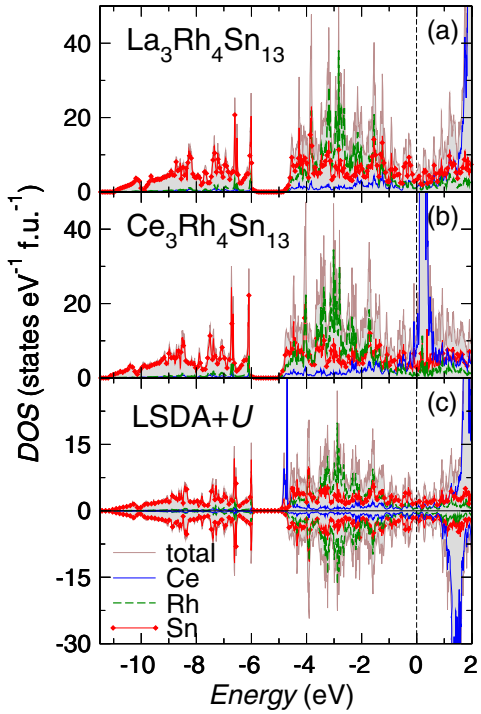

Figure 9. (Colour online) The total and atom-resolved density of states of $Ce_3Rh_4Sn_{13}$ (a) and $La_3Rh_4Sn_{13}$ (b) calculated within the LDA approximation. Panel (c) presents the total and atomic, spin-resolved density of states of $Ce_3Rh_4Sn_{13}$ calculated within the LSDA + U ($U = 6$ eV) approach applied for the Ce 4f shell. The majority (minority) spin was plotted upward (downward). The common vertical dashed line indicates the position of the Fermi level.

are formed mainly by the Ce 4f states and cross E_F due to the underestimate of Coulomb repulsion of the 4f electrons in the L(S)DA approximation. In contrast, the XPS core-level spectra as well as magnetic susceptibility data revealed a stable trivalent configuration of Ce atoms in $Ce_3Rh_4Sn_{13}$, suggesting the strongly correlated character of Ce 4f states. Therefore we applied the so-called LSDA + U approach to the Ce 4f shell in order to account for the strong Coulomb interaction in a mean-field-like (static) approximation. Inclusion of the Hubbard-like interaction term to the XC potential results in a shift of the occupied Ce 4f bands toward higher binding energies and of the unoccupied 4f states above the Fermi level. Consequently, it suppresses the incorrect hybridization between the 4f and valence band states close to the Fermi level and leads to the increase of the Ce spin moment.

Calculations with an U parameter larger than ≈4 eV yield the qualitatively correct description of trivalent Ce ions in $Ce_3Rh_4Sn_{13}$, with approximately one electron occupying the 4f shell and the Ce spin moment close to 1 μ_B. For $U \approx 6$ eV, which is typical for Ce^{3+} [39, 40], the occupied 4f states form a very narrow peak at about 4.7 eV below the Fermi level (figure 9(c)). The calculated spin moments on Rh and Sn are very small (<0.01 μ_B). Hence, in a first approximation the magnetic ground state properties of $Ce_3Rh_4Sn_{13}$ could be attributed to the RKKY type interactions among the well-localized 4f moments that couple via the itinerant electrons.

The variation of the U and J parameters in ranges of 4–8 eV and 0–1 eV, respectively, results only in an energy shift of the occupied 4f band on the energy scale. It almost does not affect the overall shape of the band structure. Moreover, the dependence on the chosen U and J values is negligible in the region close to the Fermi level which is relevant for the low-lying excitations. This justifies the application of the LSDA + U approximation.

One should note that the shape of all partial DOSs as well as the band structure, except for the 4f bands, are very similar for $La_3Rh_4Sn_{13}$ and $Ce_3Rh_4Sn_{13}$ with the Ce 4f shell treated using the LSDA + U approach. This gives further support for the picture that the Ce 4f states in $Ce_3Rh_4Sn_{13}$ are well localized.

Based on the calculated partial DOSs, we have estimated the theoretical XPS spectra, according to the description in section 2.2. The results are presented in figure 10. The most intense peak in valence band spectra located at about 3 eV originates mainly from the Rh 4d states hybridized with 5p states of Sn. The second peak centred at about 7 eV is related to photoemission from Sn 5s states. Direct comparison of the $La_3Rh_4Sn_{13}$ and $Ce_3Rh_4Sn_{13}$ XPS valence band spectra (figure 10(b)) clearly shows that there is no difference in their shape. To justify this result we illustrate the Ce 4f contribution to the XPS spectrum by plotting the partial Ce 4f DOSs as well as the sum of all partial l-resolved DOSs, multiplied by the corresponding cross sections (figures 10(c) and (d)). It is clearly visible that the Ce 4f states should give only a very small contribution to the measured spectrum, as compared to the other valence band states. Such a slight signal could not be distinctly detected. Therefore the XPS valence band spectrum of $Ce_3Rh_4Sn_{13}$ is not decisive with respect to the localization of the 4f states in the valence band. The detailed comparison of the theoretical and experimental results shows that the calculated curves reflect all features present in the measured XPS valence band spectra of both $Ce_3Rh_4Sn_{13}$ and $La_3Rh_4Sn_{13}$. The discrepancies in intensities, especially in the vicinity of the Fermi level, are often observed for Ce- and La-based intermetallics [41]. We suppose that they arise mainly from the photoemission cross sections, which in the case of the valence band states of metals might differ significantly from those obtained by Yeh and Lindau from the atomic-like calculations [22].

The 'bare' Sommerfeld coefficient calculated based on the DOS at the Fermi level amounts to 13 mJ mol^{-1} K^{-2} for both $La_3Rh_4Sn_{13}$ and $Ce_3Rh_4Sn_{13}$ (in the LSDA+U approach). For $La_3Rh_4Sn_{13}$ this value is in good agreement with that estimated from the low-temperature specific heat measurements.

Finally, we performed a computational crystal structure optimization for $Ce_3Rh_4Sn_{13}$ and $La_3Rh_4Sn_{13}$. The resulting lattice parameters and atomic coordinates are listed in table 1. The theoretical estimations are in good agreement with the experimental data for both compounds. This is in line with the conclusion that slight differences in stoichiometry, presumably related to the non-integer occupancy of the 2a position by Sn atoms, do not influence strongly the lattice parameters. Furthermore, the equilibrium unit cell volume is very similar for $Ce_3Rh_4Sn_{13}$ within the LSDA and the LSDA+U approach, which strongly indicates that the Ce 4f electrons do not contribute essentially to the chemical bonding.

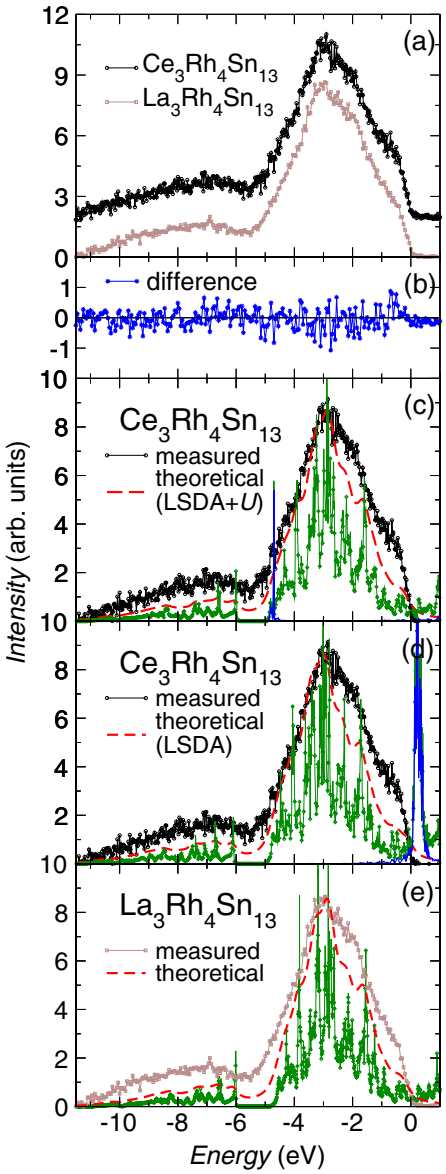

Figure 10. (Colour online) The XPS valence band spectra of $Ce_3Rh_4Sn_{13}$ and of $La_3Rh_4Sn_{13}$ (a) and their difference (b). In panels (c)–(e), the XPS valence band spectra of $Ce_3Rh_4Sn_{13}$ and of $La_3Rh_4Sn_{13}$ (background subtracted according to the Tougaard algorithm [44]) are compared with the calculated ones based on the FPLO densities of states within the LDA approximation and using the LSDA + U ($U = 6$ eV) approach for the strong Coulomb correlation within the Ce 4f shell for $Ce_3Rh_4Sn_{13}$. The thin solid (green) lines with diamonds represent the sum of the partial l-resolved DOSs multiplied by the corresponding cross sections. The thin solid (blue) lines show the partial Ce 4f contributions.

To understand the reason for formation of vacancies in the 2a atomic position we analyse charge density distribution in $RE_3Rh_4Sn_{13}$.

3.5. Charge density analysis

The bonding nature of solids can be described using electronic density plots that have been calculated in the context of a first-principles approach [42]. We derived the charge densities from band structure calculations using the WIEN2k_05 computer code [21] within the GGA approximation. We have calculated the 3D difference charge density plots between crystalline and superposed atomic densities to illustrate the reordering of electronic density accompanying the bond formation in the solid. The result for $La_3Rh_4Sn_{13}$ is shown in figure 11, but the same topology of the charge density has been found for $Ce_3Rh_4Sn_{13}$. This is expected since the Ce 4f states in this system form a very narrow band and their contribution to the chemical bonding is supposed to be negligible (see the discussion in section 3.4).

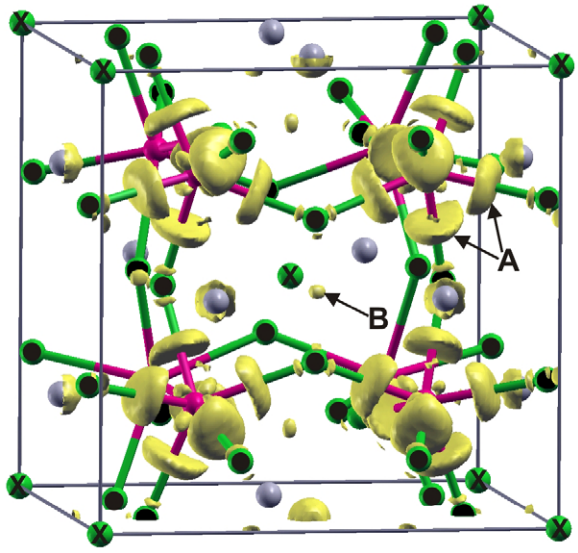

Figure 11. (Colour online) The surface of constant difference charge density equal to 0.041 (electron $Å^{-3}$). The balls represent the following atoms: Sn1—grey with black cross, Sn2—grey with black circle, La—light grey, Rh—dark grey. The strongest charge accumulations are indicated as A and B. Because of symmetry, only half of the unit cell is considered.

The compounds $RE_3Rh_4Sn_{13}$ (RE = La, Ce) crystallize in the cubic $Yb_3Rh_4Sn_{13}$-type structure which contains two different Sn sites (table 1). The Sn2 atoms form trigonal prisms around Rh. The difference charge density plot (figure 11) displays two types of charge accumulations around these atoms. The most pronounced ones are located between the nearest-neighbouring Sn2 and Rh atoms (A) pointing to the formation of the covalent-like bonds. Thus, the crystal structure can be viewed as the three-dimensional network of cornersharing $RhSn(2)_6$ prisms. This network generates two different cages occupied by RE and Sn1 atoms. The second-type charge accumulations (B) indicate that there are also multi-centre bonds between the Sn2 atoms with possible contribution from the two surrounding RE atoms and one Sn1 atom.

The electron density plots do not reveal any other covalent-like bonds formed by the Sn1 atoms in the investigated structure. Since the charge densities as well as the XPS core-level spectra do not show a significant charge transfer related to this atomic position, one can expect that the bonding at the Sn1 site have mainly metallic character.

3.6. Theoretical simulation of vacancies

The experimental indications for the non-integer occupancy of the 2a position by Sn and the dominant metallic character of the chemical bonding at this site motivated us to simulate the vacancies at this atomic position in the band structure calculations. We applied the virtual crystal approximation (VCA), which introduces virtual atoms with non-integer nuclear charge at the particular site, thus providing an effective method for studying solid solutions and alloys from first principles. This approach describes the effect of a changed chemical potential due to vacancies on an averaged level, however, neglecting effects like local distortion and disorder. The magnetic behaviour of the simulated alloys has been probed by using the fixed spin moment (FSM) method. The results are shown in figure 12.

For the stoichiometric compound $Ce_3Rh_4Sn_{13}$ the energy versus moment plot shows a broad single minimum at about 1.8 μ_B/cell. The inclusion of vacancies at the 2a site leads first to the long flat region in the calculated curves for small concentrations of vacancies (i.e. $Ce_3Rh_4Sn_{12.95}$). This indicates that the system becomes magnetically unstable. Finally, for the larger simulated concentrations of vacancies (i.e. $Ce_3Rh_4Sn_{12.9}$; $Ce_3Rh_4Sn_{12.85}$) the minimum corresponding to the magnetic ground state shifts towards higher magnetic moments and a second distinct minimum appears with a similar total energy that matches the nonmagnetic state. Further increase in the number of vacancies leads again to one magnetic minimum in the calculated FSM curves. Allowance for the lattice relaxation in the alloys almost does not influence the calculated plots.

Obviously the VCA approach provides only a rough approximation for the simulation of vacancies. For more detailed studies one should use more sophisticated computational methods (e.g. the coherent potential approximation). The lowering of the symmetry, required by the possible antiferro- or ferrimagnetic spin arrangement, could also affect slightly the calculated total energy curves. Nevertheless, our studies clearly show that the magnetic properties of the $Ce_3Rh_4Sn_{13}$ system strongly depend on the local composition.

3.7. Discussion

At room temperature $Ce_3Rh_4Sn_{13}$ behaves like an ordinary paramagnet with the full moment expected for Ce^{3+} ions. At lower temperatures, the crystal field splitting of the $J = 5/2$ Hund's rule multiplet becomes important and strongly modifies the thermodynamic properties. The crystal field level scheme derived from specific heat (three doublets, $\Delta_1/k_B \approx 95$ K, $\Delta_2/k_B \approx 350$ K) is consistent with that obtained from inelastic neutron scattering [24]. Although there are some indications for a Kondo effect in resistivity and magnetic susceptibility data, the Kondo temperature is supposed to be low. Further, the low-temperature susceptibility data point to weak exchange interactions corresponding to the ground state doublet, in agreement with results of *ab initio* band structure calculations. Thus, the compound $Ce_3Rh_4Sn_{13}$ can be assigned to the weakly coupled part of the Doniach phase diagram [5].

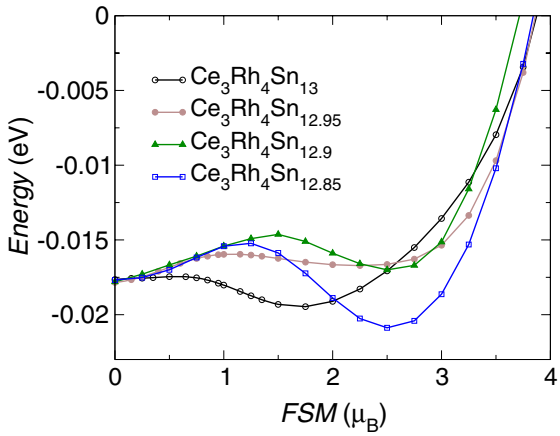

Figure 12. (Colour online) The total energy versus FSM curves derived from fixed spin moment calculations for different compositions of the $Ce_3Rh_4Sn_{13}$-type systems simulated using the VCA approach. The total energy scales for different curves were shifted to show the same value for the nonmagnetic state. The FSM values represent the total magnetic moments calculated per unit cell.

The theoretical simulation presented in section 3.6 provides an explanation for the discrepancy in magnetic ground state properties between different $Ce_3Rh_4Sn_{13}$ samples. It is worthwhile to stress that Ōduchi *et al* [10] found two magnetic phase transitions at $T_{N1} = 1.2$ K and $T_{N2} = 2.0$ K using a crystal obtained by the self-flux method from Sn as flux. This finding is in line with a magnetic ground state predicted by the band structure calculations for the stoichiometric $Ce_3Rh_4Sn_{13}$. In contrast, polycrystals (reported here and from reference [11]) do not show any sign of a long-range magnetic order in this temperature range. In view of our theoretical results the short-range magnetic ordering at the temperature of 1 K [11] could be attributed to the slight non-stoichiometry and disorder in the sample. It should be pointed out that the investigated polycrystalline materials were obtained from stoichiometric amounts of the elemental metals and were found to contain some traces of Sn ($\leqslant$2%) after the melting and annealing procedure. One should note that the presence of 1% Sn impurities in the sample implies the composition of the main phase $Ce_3Rh_4Sn_{12.8}$ which corroborates the presented analysis. Such slight differences in composition are close to the present resolution of a careful WDX analysis. The theoretical calculations indicate that the magnetic ground state properties are influenced significantly even by Sn defects of the order of 0.1 at.%.

They should, however, strongly influence the measured resistivity curves first of all due to the changes in magnetic scattering. Indeed, there are substantial discrepancies in both the temperature and field dependence of electrical resistivity for the compound $Ce_3Rh_4Sn_{13}$ between the data obtained by different research groups [11, 9] as well as the results reported here. Furthermore, all the reported resistivity curves show only a weak temperature dependence over a wide temperature range and high absolute values of the order of 150–300 $\mu\Omega$ cm, which corroborates the strong magnetic disorder effects in the investigated samples. For comparison, the nonmagnetic system

$La_3Rh_4Sn_{13}$ shows metallic behaviour and an overall shape of the resistivity curve which is similar to those previously published [11]. One should also note that the absolute values of the resistivity of $La_3Rh_4Sn_{13}$ at temperatures above the superconducting phase transition are much lower than those for $Ce_3Rh_4Sn_{13}$.

At this moment, the mechanism leading to the significant positive magnetoresistance for $Ce_3Rh_4Sn_{13}$ at temperatures below ≈50 K is not clear. One should note that Köhler *et al* [11] found a negative magnetoresistance for $Ce_3Rh_4Sn_{13}$ at low temperatures, which again points to the strong sample dependence. Hence, one can associate this effect with the slight non-stoichiometry and inhomogeneity of the polycrystalline sample. A positive magnetoresistivity could result from the so-called magnetic precursor effect, originally proposed to explain anomalous thermodynamic and transport properties of some Gd-based intermetallics [25]. According to Mallik *et al* [25], in some metallic materials a magnetic disorder-induced localization of electrons can develop far before a magnetic order sets in. This process may give rise to the appearance of a significant magnetic contribution to the electrical resistivity and heat capacity at temperatures much above magnetic ordering. In the case of antiferromagnetic-type systems such a localization implies a positive magnetoresistivity.

Finally one should note that the broad maximum in zero-field resistivity of $Ce_3Rh_4Sn_{13}$ at the temperature of 30 K might resemble the coherence effect, as often observed in Ce-based Kondo lattice systems at temperatures lower than the Kondo energy scale. Then, the increase in resistivity with applied magnetic field at temperatures below the maximum would result from the destruction of the coherence between Kondo impurities by external magnetic field [43]. This mechanism, however, seems to be unlikely for $Ce_3Rh_4Sn_{13}$ due to the anticipated low Kondo temperature. Moreover, a substantial amount of disorder found in the polycrystalline sample is expected to prevent the formation of the coherence state.

4. Conclusion

We presented combined studies of the electronic structure and the thermodynamic properties of the compounds $Ce_3Rh_4Sn_{13}$ and $La_3Rh_4Sn_{13}$. The Ce 3d and 4d XPS spectra point to a stable configuration of the Ce 4f shell in $Ce_3Rh_4Sn_{13}$ and a rather weak hybridization Δ of the Ce 4f and conduction band states with $\Delta \approx 35$ meV. The stable Ce^{3+} valence is consistent with magnetic susceptibility measurements and the results of the computational crystal structure optimization, which indicate that there is no significant contribution of the Ce 4f electrons to the chemical bonding in $Ce_3Rh_4Sn_{13}$. The electronic structure of $Ce_3Rh_4Sn_{13}$ calculated within the LSDA + U approach is very similar to that of the reference compound $La_3Rh_4Sn_{13}$, which in combination with the XPS spectra strongly suggests that the Ce 4f states are well localized in $Ce_3Rh_4Sn_{13}$.

The low-temperature thermodynamic properties of $Ce_3Rh_4Sn_{13}$ are determined by the strong crystal field splitting of the $J = 5/2$ multiplet into three doublets. The two excited states are found to be separated from the ground state by $\Delta_1/k_B \approx 95$ K and $\Delta_2/k_B \approx 350$ K. We did not find any evidence for long-range magnetic ordering in $Ce_3Rh_4Sn_{13}$ above 1.8 K, in contrast to the recent report [10]. Instead, the resistivity curves point to the substantial amount of disorder and structural defects in both $Ce_3Rh_4Sn_{13}$ and $La_3Rh_4Sn_{13}$ as well as the strong magnetic disorder effects in the polycrystalline sample of $Ce_3Rh_4Sn_{13}$. For $La_3Rh_4Sn_{13}$, the thermodynamic data revealed an intrinsic superconducting transition at 2.07 K. This critical temperature differs markedly from those previously reported (3.8 K [11]; 3.0–3.2 K [12]; 2.9 K [10]).

The determination of the chemical composition of our polycrystalline samples shows that they are very close to the stoichiometric composition, but it does not exclude small deviation in Sn content. Variation of the reported lattice parameters (table 1) and the partial occupancy of the 2a position in the published structure model [6] point to a small homogeneity range. Theoretical simulation of vacancies at the 2a atomic position within the VCA approximation revealed that the magnetic ground state of $Ce_3Rh_4Sn_{13}$ is very sensitive to the Sn content. Thus, slight non-homogeneity or non-stoichiometry of the sample can result in different magnetic properties.

Single crystals of well-defined stoichiometry should be synthesized to reduce the disorder-induced effects. Further studies on such crystals are required to clarify the low-temperature energy scales for the compound $Ce_3Rh_4Sn_{13}$ as well as the superconducting critical temperature of $La_3Rh_4Sn_{13}$.

Acknowledgments

The authors thank Ulrike Köhler for discussions and critical remarks. The authors also thank the financial support from project nos. 1 P03B 052 28 and N202 010 32/0487 of the Ministry of Science and Higher Education and for the DFG Emmy Noether programme.

References

[1] Jeitschko W and Braun D 1977 *Acta Crystallogr.* B **33** 3401
[2] Takayanagi S, Sato H, Fukuhara T and Wada N 1994 *Physica* B **199/200** 49–51
Nagoshi C, Sugawara H, Aoki Y, Sakai S, Kohgi M, Sato H, Onimaru T and Sakakibara T 2005 *Physica* B **359–361** 248–50
[3] Cornelius A L, Christianson A D, Lawrence J L, Fritsch V, Bauer E D, Sarrao J L, Thompson J D and Pagliuso P G 2006 *Physica* B **378–380** 113
Christianson A D, Gardner J S, Kang H J, Chung J-H, Bobev S, Sarrao J L and Lawrence J M 2007 *J. Magn. Magn. Mater.* **310** 266
[4] Sokolov D A, Aronson M C, Henderson C and Kampf J W 2007 *Phys. Rev.* B **76** 075109
[5] Doniach S 1997 *Physica* B **91** 231
[6] Patil N G and Ramakrishnan S 1997 *Phys. Rev.* B **56** 3360
[7] Miraglia S, Hodeau J L, Marezio M, Laviron C, Ghedira M and Espinosa G P 1986 *J. Solid State Chem.* **63** 358
[8] Hodeau J L, Marezio M, Remeika J P and Chen C H 1982 *Solid State Commun.* **42** 97
[9] Niepmann D, Pöttgen R, Poduska K M, DiSalvo F J, Trill H and Mosel B D 2001 *Z. Naturforsch.* B **56** 1–8

[10] Ōduchi Y, Tonohiro C, Thamizhavel A, Nakashima H, Morimoto S, Matsuda T D, Haga Y, Sugiyama K, Takeuchi T, Settai R, Hagiwara M and Ōnuki Y 2007 *J. Magn. Magn. Mater.* **310** 249
[11] Köhler U, Pikul A P, Oeschler N, Westerkamp T, Strydom A M and Steglich F 2007 *J. Phys.: Condens. Matter* **19** 386207
[12] Espinosa G P, Cooper A S and Barz H 1982 *Mater. Res. Bull.* **17** 963
Remeika J P, Espinosa G P, Cooper A S, Barz H, Rowell J M, McWhan D B, Vandenberg J M, Moncton D E, Fisk Z, Woolf L D, Hamaker H C, Maple M B, Shirane G and Thomlinson W 1980 *Solid State Commun.* **34** 923
[13] Krauss W and Nolze G 1996 *J. Appl. Crystallogr.* **29** 301
[14] Akselrud L G, Zavalii P Y, Grin Yu, Pecharsky V K, Baumgartner B and Wölfel E 1993 *Mater. Sci. Forum* **133–136** 335
[15] Baer Y, Bush G and Cohn P 1975 *Rev. Sci. Instrum.* **46** 466
[16] Koepernik K and Eschrig H 1999 *Phys. Rev.* B **59** 1743
[17] Perdew J P and Wang Y 1992 *Phys. Rev.* B **45** 13244
[18] Eschrig H 1989 *Optimized LCAO Method and the Electronic Structure of Extended Systems* (Berlin: Springer)
[19] Eschrig H, Koepernik K and Chaplygin I 2003 *J. Solid State Chem.* **176** 482
[20] Singh D 1994 *Plane Waves, Pseudopotentials and the LAPW Method* (Boston: Kluwer Academic)
[21] Blaha P, Schwarz K, Madsen G, Kvasnicka D and Luitz J 2001 *WIEN2k, Program for Calculating Crystal Properties* Vienna University of Technology (ISBN 3-9501031-1-2)
[22] Yeh J J and Lindau J 1985 *At. Data Nucl. Data Tables* **32** 1
[23] Bordet P, Cox D E, Espinosa G P, Hodeau J L and Marezio M 1991 *Solid State Commun.* **78** 359 and references there in
[24] Adroja D T, Strydom A M, Murani A P, Kockelmann W A and Fraile A 2008 *Physica* B **403** 898
[25] Mallik R and Sampathkumaran E V 1998 *Phys. Rev.* B **58** 9178
Mallik R, Sampathkumaran E V, Strecker M and Wortmann G 1998 *Europhys. Lett.* **41** 315
[26] Gamża M, Ślebarski A and Rosner H 2008 *J. Phys.: Condens. Matter* **20** 025201
[27] Ślebarski A, Spałek J, Gamża M and Hackemer A 2006 *Phys. Rev.* B **73** 205115
[28] Selwood P W 1956 *Magnetochemistry* (New York: Interscience)
[29] Mott N F 1935 *Proc. R. Soc.* A **153** 699
Calandra M and Gunnarsson O 2002 *Phys. Rev.* B **66** 205105
[30] Cornut B and Coqblin B 1972 *Phys. Rev.* B **5** 4541
[31] Fuggle J C, Gunnarsson O, Sawatzky G A and Schönhammer K 1988 *Phys. Rev.* B **37** 1103
[32] Gamża M, Ślebarski A and Rosner H 2008 *Eur. Phys. J.* B **63** 1
[33] Baer Y, Hauger R, Zürcher Ch, Campagna M and Wertheim G K 1978 *Phys. Rev.* B **18** 4433
[34] Fuggle J C, Hillebrecht F U, Zolnierek Z, Lässer R, Freiburg Ch, Gunnarsson O and Schönhammer K 1973 *Phys. Rev.* B **27** 7330
[35] Signorelli A J and Hayes R G 1973 *Phys. Rev.* B **8** 81
[36] Gunnarsson O and Schönhammer K 1983 *Phys. Rev.* B **28** 4315
[37] Ślebarski A, Maple M B, Freeman E J, Sirvent C, Radłowska M, Jezierski A, Granado E, Huang Q and Lynn J W 2002 *Phil. Mag.* B **82** 943
Ślebarski A, Jezierski A, Zygmunt A, Mähl S and Neumann M 1998 *Phys. Rev.* B **58** 13498
[38] Lässer R, Fuggle J C, Bryss M, Campagna M, Steglich F and Hulliger F 1980 *Physica* B **102** 360
Campagna M and Hillebrecht F U 1987 *Handbook on the Physics and Chemistry of Rare Earths* vol 10, ed K A Gschneidner, L Eyring Jr and S Hüfner, p 75
Kang J-S, Allen J W, Gunnarsson O, Christensen N E, Andersen O K, Lassailly Y, Maple M B and Torikachvili M S 1990 *Phys. Rev.* B **41** 6610
Steglich F, Aarts J, Bredl C D, Lieke W, Meschede D, Franz W and Schäfer H 1979 *Phys. Rev. Lett.* **43** 1892
[39] Boring A M, Albers R C, Eriksson O and Koelling D D 1992 *Phys. Rev. Lett.* **68** 2652
Herbst J F, Watson R E and Wilkins J W 1978 *Phys. Rev.* B **17** 3089
Herbst J F and Wilkins J W 1979 *Phys. Rev. Lett.* **43** 1760
Anisimov V I and Gunnarsson O 1991 *Phys. Rev.* B **43** 7570 and references therein
[40] Allen J W, Oh S-J, Gunnarsson O, Schönhammer K, Maple M B, Torikachvili M S and Lindau I 1986 *Adv. Phys.* **35** 275
Lang J K, Baer Y and Cox P A 1981 *J. Phys. F: Met. Phys.* **11** 121
[41] Gamża M, Ślebarski A and Deniszczyk J 2008 *J. Phys.: Condens. Matter* **20** 025201
[42] Gelatt C D, Williams A R Jr and Moruzzi V L 1983 *Phys. Rev.* B **27** 2005
[43] Cox D L and Grewe N 1988 *Z. Phys.* B **71** 321
[44] Tougaard S and Sigmund P 1982 *Phys. Rev.* B **25** 4452